JOURNAL OF PETROLOGY | VOLUME 54 | NUMBER 5 | PAGES 933–949 | 2013 | doi:10.1093/petrology/egt001

Calibration of an Empirical Thermometer and Oxybarometer based on the Partitioning of Sc, Y and V between Olivine and Silicate Melt

GUILHERME MALLMANN[1]* AND HUGH ST.C. O'NEILL[2]

[1]INSTITUTO DE GEOCIÊNCIAS, UNIVERSIDADE DE SÃO PAULO, SÃO PAULO, SP 05508-080, BRAZIL

[2]RESEARCH SCHOOL OF EARTH SCIENCES, AUSTRALIAN NATIONAL UNIVERSITY, CANBERRA, ACT 0200, AUSTRALIA

RECEIVED AUGUST 13, 2012; ACCEPTED DECEMBER 31, 2012
ADVANCE ACCESS PUBLICATION FEBRUARY 7, 2013

The evolution of basaltic magmas depends on their redox state, hence oxygen fugacity, but there is increasing evidence that this intensive thermodynamic variable may be less well understood in basalts than commonly supposed. The redox state of terrestrial basalts has to a large extent been inferred from the Fe^{3+}/Fe^{2+} ratios of their quenched glasses. However, this quantity appears to be significantly affected during late and post-eruptive processes in magmatic systems (e.g. by degassing, charge-transfer reactions of redox-variable species, and alteration), so that the degree to which the Fe^{3+}/Fe^{2+} ratios preserved in basaltic glasses reflect the oxidation state of the magma at high temperature is unclear. Because olivine is the first silicate mineral to crystallize from primitive basaltic liquids on cooling following decompression, the equilibrium partitioning relations preserved in olivine phenocrysts in basalts are, in principle, less disturbed by these late and post-eruptive processes and, therefore, may better reflect the high-temperature (pre-eruptive) conditions of the magma. Here we calibrate an oxybarometer based on the strong sensitivity of the partitioning of vanadium between olivine and silicate melt to oxygen fugacity. Our empirical parameterization, calibrated over a range of redox conditions between four log_{10} units above and below the quartz–fayalite–magnetite (QFM) oxygen buffer, takes into account the effects of temperature, olivine composition (i.e. Mg/Fe ratios) and melt composition (namely the activities of CaO, SiO_2, $AlO_{1.5}$, $NaO_{0.5}$ and $KO_{0.5}$), and allows oxygen fugacity determinations to within ~0·25 log_{10} units. We also explore the sensitivity of the exchange partitioning of Sc and Y between olivine and melt to temperature as a geothermometer. Our calibration indicates that this geothermometer allows temperature to be estimated to within 15°C, but precision is strongly dependent on the Sc and Y measurements in olivine and melt.

KEY WORDS: *olivine; basalt; temperature; oxygen fugacity; trace element*

INTRODUCTION

The course of evolution of basaltic magmas depends on their redox state, hence oxygen fugacity (f_{O_2}). However, there is increasing evidence that this intensive thermodynamic variable may be less well known in basalts than commonly supposed. The redox state of terrestrial basalts has to a large extent been inferred from the Fe^{3+}/Fe^{2+} ratios of their quenched glasses, but the recent XANES (X-ray absorption near-edge structure) spectroscopy determinations of Fe^{3+}/Fe^{2+} in mid-ocean ridge basalt (MORB) glasses of Cottrell & Kelley (2011) differ from the earlier wet-chemical measurements of either Christie *et al.* (1986) or Bézos & Humler (2005). The degree to which the Fe^{3+}/Fe^{2+} ratios preserved in silicate glasses reflect the oxidation state of the magma at high temperature is also unclear. A severe problem is the degassing of volatiles species, particularly those containing sulfur (e.g. Burgisser & Scaillet, 2007; Métrich *et al.*, 2009). Even for nearly undegassed basalts such as MORB, which mostly retain their original sulfur contents, the extent to which wet-chemical methods are systematically biased by reduction of dissolved sulfide (S^{2-}) has not yet been fully evaluated (e.g. Sossi & O'Neill, 2011). Although Fe is by far the most abundant redox-variable element in basalts, temperature-dependent charge-transfer (also known as electron-exchange) reactions between Fe^{3+}/Fe^{2+} and other

*Corresponding author. E-mail: guil.mallmann@gmail.com

redox-variable elements such as Cr^{2+}/Cr^{3+} (e.g. Berry *et al.*, 2003) and S^{2-}/SO_4^{2-} (e.g. Métrich *et al.*, 2009) may alter the valence states of these species during the quenching of magmas. Recent evidence from bulk-rock V/Sc and Zn/Fe ratios, as well as Cu systematics and Fe isotopes (Lee *et al.*, 2005, 2010, 2012; Dauphas *et al.*, 2009; Mallmann & O'Neill, 2009), also indicates that the sources of primitive island arc basalts (IAB) may have oxidation states similar to those of MORB, an observation that runs against the commonly held view that subduction of oceanic crust, which may introduce oxidizing components to the mantle beneath arcs (Evans, 2012), causes partial melting of the mantle under more oxidizing conditions than at mid-ocean ridges.

Here we present new experimental data on the partitioning of the redox-sensitive element vanadium between olivine and silicate melt ($D_V^{ol/melt}$), to allow an improved calibration of the $D_V^{ol/melt}$ oxybarometer as an alternative means of estimating oxygen fugacity in basalts. Olivine is the first silicate mineral to crystallize from primitive basaltic liquids on cooling following decompression. Therefore, the equilibrium partitioning relations preserved in olivine phenocrysts in basalts are, in principle, less disturbed by late-stage magmatic processes (e.g. degassing, charge-transfer reactions, and alteration), which obscure the interpretation of Fe^{3+}/Fe^{2+} of basaltic rocks and glasses. The use of $D_V^{ol/melt}$ to measure oxygen fugacity in magmas has previously been promoted by Canil (1997, 2002), Canil & Fedortchouk (2001), Shearer *et al.* (2006) and Mallmann & O'Neill (2009), but these preliminary calibrations did not address the effects of composition, temperature and pressure.

Trace-element partitioning between olivine and melt also offers opportunities of developing alternative geothermometers, and here we show that the exchange of Sc with Y between olivine and melt has good sensitivity to temperature with a sufficiently modest dependence on other variables (i.e. melt composition, olivine composition, and pressure) to be a practical geothermometer. Essential to the success of these methods are recent advances in trace-element microanalysis, particularly laser ablation inductively coupled plasma mass spectrometry (LA-ICP-MS), which have allowed the determination of incompatible trace element contents in natural olivines to the kind of precisions useful for quantitative petrological inferences (e.g. Witt-Eickschen & O'Neill, 2005; De Hoog *et al.*, 2010; Foley *et al.*, 2011).

In the course of this study we also determined partition coefficients between olivine and silicate melt for a range of other trace elements [Na, Al, Ca, Ti, Cr, Mn, Zr, and the heavy rare earth elements (REE) Tb, Er and Yb]. The partitioning relations of some of these elements are also of potential usefulness to the understanding of olivine-phyric basaltic rocks, but their modes of substitution into olivine are probably complex and will be discussed in detail elsewhere.

EXPERIMENTAL METHODS

Three 'parent' starting compositions, from which several other 'daughter' compositions were derived, were studied. These starting compositions were chosen to complement the experimental data already obtained on olivine/melt partitioning relations in previous studies from our laboratory (Mallmann & O'Neill, 2007, 2009; Evans *et al.*, 2008; Tuff & O'Neill, 2010). Since this previous work has focused either on Fe-free compositions (e.g. Evans *et al.*, 2008) or on compositions with constant Mg/Fe (e.g. Tuff & O'Neill, 2010), a special effort was made to produce compositions covering a large range of Fe/Mg ratios. Fe-free compositions were also studied because they allow the effect of melt composition alone on olivine/melt partitioning to be investigated, given that olivine becomes a phase of almost fixed major element composition (i.e. Mg_2SiO_4) in Fe-free systems. The effects of alkalis (Na and K), which are volatile at high temperature and atmospheric pressure and therefore subject to progressive loss during an experiment, were assessed using the method for controlling alkali–metal oxide activities described by O'Neill (2005).

The first 'parent' composition (DFA) used in this study is based on the intersection of the forsterite primary crystallization volume with the 1400°C isotherm in the subsystem Mg_2SiO_4–$Mg_2Si_2O_6$–$CaMgSi_2O_6$ (Evans *et al.*, 2008). Variable amounts (up to 18 cg g^{-1}) of Al_2O_3 were added to this composition to make up a subset of seven 'daughter' compositions in the CMAS system. Adding variable amounts of fayalite (Fe_2SiO_4) plus FeO to DFA produced another subset of seven 'daughter' compositions in the FCMS system. The second 'parent' composition (MORB-ol; $SiO_2 = 54{\cdot}9$, $TiO_2 = 1{\cdot}72$, $Al_2O_3 = 23{\cdot}0$, $CaO = 16{\cdot}5$, $MnO = 0{\cdot}37$, and $Na_2O = 3{\cdot}51$ in cg g^{-1}) is based on that of mid-ocean ridge basalts to which variable amounts of olivine-composition oxide mixes (ranging from Fo_{100} to Fo_{40}) were added to produce seven 'daughter' compositions. The amount of olivine and FeO added to the MORB-ol and DFA 'parent' compositions was varied based on experience to produce 'daughter' compositions crystallizing ~10–30 vol. % of olivine. The third 'parent' composition (M666) is based on the chilled margin of a komatiite flow from Alexo (Canada) reported by Arndt (1986). This composition allows olivine/melt partitioning to be investigated to higher temperatures. All compositions were prepared from reagent grade oxides and carbonates, and doped with nominal concentrations of Sc, V, Cr, Y, Zr, Tb, Er and Yb, added as oxide powders, between 150 and 4000 μg g^{-1}.

Charges for one atmosphere (1 bar) experiments were prepared by mixing about 100 mg of powder of each composition with polyethylene oxide and mounting the

resulting sludge on either Pt, Pd, Re or Ir wire loops; the choice of wire depends on the target oxygen fugacity of a particular experiment. Up to seven compositions could be run at a time with wire loops suspended from a Pt 'chandelier'. The samples were introduced in the furnace at 600°C and the temperature was increased at a rate of 6°C min^{-1}. Some experiments were initially held for a few hours above (or near) the liquidus temperature and then cooled over a few minutes (as fast as the furnace allowed) to the intended run temperature to produce larger crystals for laser ablation analyses. The equilibrium temperature, which varied from 1200 to 1530°C, was then held for 8–288 h. All 1 bar experiments were carried out in vertical tube furnaces equipped for gas mixing at the Research School of Earth Sciences, Australian National University. Oxygen fugacity was set by $CO–CO_2$ gas mixing, with gas flows controlled by Tylan mass flow controllers of 0–10 and 0–200 standard cubic centimeter per minute (sccm) flow range. Oxygen fugacity at a given temperature was calculated using the thermodynamic data for gas species in the NIST-JANAF tables (Chase, 1998). Temperature was controlled by a type B thermocouple external to the muffle tube feeding into a Eurotherm controller, and in most cases was also independently measured by a second internal type B thermocouple placed immediately above the samples. Accuracy is expected to be better than 5°C. Runs were terminated by drop-quenching into water, resulting in liquids quenching to glasses for most compositions (even the komatiitic compositions), except the two highest Fe samples in run B05/04/11 (#6 and #7), which formed a microcrystalline matrix upon quenching. A summary of experimental conditions for 1 bar experiments is presented in Table 1.

Additional experiments were undertaken to assess the effect of pressure on the partitioning of trace elements between olivine and melt. These experiments used an end-loaded piston-cylinder apparatus at the Research School of Earth Sciences, Australian National University, with $\frac{1}{2}$ inch NaCl–Pyrex–graphite–MgO pressure cells. Temperature was monitored by type B thermocouples. Three experiments, which have not been buffered for oxygen fugacity, were conducted with the M666 composition containing 5–8 cg g^{-1} of H_2O at 0·5 GPa in AuPd capsules. However, these experiments ended without significant H_2O owing to H_2 loss through the capsules, as indicated by the near 100% total of the glass analyses and very low $D_V^{ol/melt}$ (which implies very oxidizing conditions; see further discussion). One experiment was conducted with a CMAS composition in a Pt capsule at 2 GPa, and three more experiments with a MORB-ol + Fo_{100} composition (undecarbonated) at pressures of 0·5, 1 and 1·5 GPa in graphite-lined Pt capsules. These latter experiments have oxygen fugacity set by the graphite–CO_2 (GCO) oxygen buffer, according to the reaction $C + O_2 = CO_2$. At saturation with a pure CO_2 vapor, $p(CO_2)$ equals the experimental pressure, P. The log f_{O_2} may be calculated from equation (7) of Frost & Wood (1997), as corrected by Frost (1998). Experimentally, this buffer was implemented by running the charge in a graphite capsule sealed inside a Pt capsule, with starting material made from an oxide–carbonate mix as usual but without prior decarbonation. A summary of experimental conditions for piston-cylinder experiments is presented in Table 2.

ANALYTICAL METHODS

Recovered experimental charges were mounted in epoxy resin, polished, and then etched and cleaned for a few minutes in an ultrasonic bath with a dilute (1:10) solution of Citranox in distilled water to reveal better the crystals at the surface in reflected light. The major and trace element composition of experimental run products were analyzed by a Cameca SX100 electron microprobe, and by LA-ICP-MS using a 193 nm ArF excimer (Lambda Physik LPX120i) LA system coupled to a quadrupole Agilent 7700s ICP-MS system, respectively. The interface between the LA and ICP-MS systems was made via a second-generation custom-built 'HelEx' two-volume vortex sampling cell (Eggins *et al.*, 1998). All instruments are housed at the Research School of Earth Sciences, Australian National University.

Electron microprobe analyses were undertaken in wavelength-dispersive mode (WDS) under routine conditions (15 kV acceleration voltage, 10–20 nA beam current, and >20 s counting times on element peaks). Olivine crystals were analyzed under a focused 1 μm beam at 20 nA, whereas glasses were analyzed under a defocused 10 μm at 10 nA. For samples B05/04/11-6 and B05/04/11-7, in which silicate melts quenched to a microcrystalline mass rather than a glass, we broadened the electron beam to cover an excitation area at the surface of ~50 μm × 50 μm. We typically collected 3–8 measurements on olivines and silicate glasses and averaged the results. San Carlos olivine and the VG-2 natural basaltic glass were used as secondary standards to monitor accuracy and reproducibility. Concentrations of all major elements determined on the VG-2 glass and San Carlos olivine are within 1% and 2%, respectively, of certified values reported by Jarosewich *et al.* (1980). Na_2O concentrations determined in the VG-2 glass show the greatest variability among the elements with contents above 1 cg g^{-1}, most probably owing to the well-known problem of alkali loss during electron-beam microanalyses. In all modeling presented in this paper, we have used the Na concentrations determined by LA-ICP-MS.

LA-ICP-MS analyses of ^{23}Na, ^{24}Mg, ^{27}Al, ^{29}Si, ^{43}Ca, ^{45}Sc, ^{47}Ti, ^{51}V, ^{53}Cr, ^{55}Mn, ^{57}Fe, ^{89}Y, ^{90}Zr, ^{159}Tb, ^{166}Er and ^{172}Yb were performed in a He atmosphere with the addition of Ar and He above the ablation site and outside the

Table 1: Summary of experimental conditions for 1 bar experiments

Experiment	Compositions	No. of samples	T (°C)	t (h)	Wire	CO_2 (sccm)	CO (sccm)	log fO_2	ΔQFM	ΔNNO
B05/04/11	DFA + Fa-FeO	7	1400	96	Pt	200·00	4·00	−5·21	1·10	0·56
C04/04/11*	DFA + 0–18% Al_2O_3	7	1375	200	Pt	54·00	26·00	−8·24	−1·69	−2·25
B28/03/11	DFA + 0–18% Al_2O_3	7	1395	186	Pt	80·00	4·00	−6·06	0·29	−0·24
B21/03/11	DFA + 0–18% Al_2O_3	7	1400	140	Pt	54·00	26·00	−7·97	−1·67	−2·20
B27/01/11	MORB-ol + Fo_{100-40}	3	1200	230	Pd	200·00	1·00	−6·38	2·03	1·36
B16/01/11	MORB-ol + Fo_{100-40}	4	1240	184	Re	54·00	26·00	−9·82	−1·87	−2·52
B04/03/11	MORB-ol + Fo_{100-40}	6	1240	216	Pd	200·00	1·00	−5·85	2·10	1·45
C15/03/11*	MORB-ol + Fo_{100-40}	7	1245	63	Re	40·00	60·00	−10·75	−2·85	−3·50
C10/03/11*	MORB-ol + Fo_{100-40}	7	1245	112	Pd	100·00	5·00	−7·79	0·11	−0·54
C12/01/11	MORB-ol + Fo_{100-40}	4	1250	288	Pd	80·00	4·00	−7·73	0·11	−0·53
B19/02/11	MORB-ol + Fo_{100-40}	4	1290	192	Re	54·00	26·00	−9·20	−1·80	−2·41
B15/03/11	MORB-ol + Fo_{100-40}	3	1300	144	Re	54·00	26·00	−9·08	−1·78	−2·39
C09/07/09†	M666 komatiite	1	1400	92	Re/Pt	40·00	10·00	−7·40	−1·09	−1·63
C13/07/09†	M666 komatiite	1	1452	41	Re/Pt	40·00	10·00	−6·88	−1·05	−1·54
C09/08/09	M666 komatiite	1	1480	15	Re/Pt	40·00	10·00	−6·61	−1·03	−1·50
C16/07/09†	M666 komatiite	1	1494	29	Re/Pt	40·00	10·00	−6·47	−1·02	−1·47
C28/07/09A	M666 komatiite	1	1520	8	Ir	40·00	10·00	−6·24	−1·01	−1·43
C28/07/09B	M666 komatiite	1	1520	8	Re/Pt	40·00	10·00	−6·24	−1·01	−1·43
C07/08/09	M666 komatiite	1	1524	8	Re	20·00	20·00	−7·81	−2·61	−3·03
C08/08/09	M666 komatiite	1	1527	6	Ir	40·00	2·00	−4·78	0·39	−0·03
B16/09/09‡	M666 komatiite	1	1530	18	Ir	25·60	0·88	−6·73	−1·58	−2·00
C05/02/10	M666 komatiite	1	1377	69	Ir	60·00	—	−3·15	3·38	2·82
C15/01/10	M666 komatiite	1	1404	97	Ir	60·00	—	−3·06	3·21	2·68
C19/01/10	M666 komatiite	1	1430	67	Ir	60·00	—	−2·97	3·06	2·55
C22/01/10	M666 komatiite	1	1482	69	Ir	60·00	—	−2·80	2·76	2·30

All experiments were conducted at atmospheric pressure in vertical tube furnaces. Quartz–fayalite–magnetite (QFM) buffer from O'Neill (1987); Ni–NiO (NNO) buffer from O'Neill & Pownceby (1993).
*Na flux.
†K flux.
‡Log $fS_2 = -1·04$.

Table 2: Summary of experimental conditions for piston-cylinder experiments

Experiment	Compositions	P (GPa)	T (°C)	t (h)	Capsule	Oxygen buffer	log fO_2	ΔQFM	ΔNNO
C4036	M666 komatiite + 5 cg g^{-1} H_2O	0·5	1250	72	AuPd	unbuffered	–	–	–
C4033	M666 komatiite + 5 cg g^{-1} H_2O	0·5	1300	8	AuPd	unbuffered	–	–	–
C4038	M666 komatiite + 8 cg g^{-1} H_2O	0·5	1350	8	AuPd	unbuffered	–	–	–
D1264	CMAS + Sc&Y	2·0	1450	24	Pt	unbuffered	–	–	–
C4240	MORB-ol + Fo_{100}	0·5	1400	24	Pt–graphite	graphite–CO_2*	−7·91	−1·60	−2·14
C4234	MORB-ol + Fo_{100}	1·0	1400	24	Pt–graphite	graphite–CO_2*	−7·53	−1·22	−1·76
C4241	MORB-ol + Fo_{100}	1·5	1400	24	Pt–graphite	graphite–CO_2*	−7·17	−0·86	−1·40

*Oxygen fugacity at P and T calculated according to the expression of Frost & Wood (1997) corrected in Frost (1998).

sample cell, respectively. Machine settings were optimized to reduce oxide production by achieving a ThO^+ signal intensity of less than 0·6% of the Th^+ signal. The laser was run at 5 Hz and constant voltage to achieve energies between 40 and 55 mJ. Spot sizes were chosen based on restrictions imposed by the size of olivines. For most experiments, we used a 22 μm spot, but in the case of samples produced by the M666 composition, we used a 16 μm spot. Identical spot sizes were used for each olivine–melt pair. For each time-resolved analysis, we acquired 20 s of background signal (laser off) followed by 40 s of ablation signal (laser on). The SRM NIST 610 silicate glass was used as external standard, assuming the following element concentrations (GeoREM database, 2006): $Na_2O = 13·4$, $Al_2O_3 = 2·04$, $SiO_2 = 70·0$ and $CaO = 11·5$ (cg g^{-1}); and Mg = 465, Sc = 441, Ti = 434, V = 442, Cr = 405, Mn = 485, Fe = 458, Y = 450, Zr = 440, Tb = 443, Er = 426 and Yb = 445 (μg g^{-1}). To correct for differences in ablation efficiency between external standard and unknowns, ^{29}Si was used as the internal reference isotope based on the concentrations of SiO_2 determined by electron microprobe or, in the case of olivines produced from Fe-free compositions, the stoichiometric SiO_2 of Mg_2SiO_4 (i.e. 42·7 cg g^{-1}). The concentrations of Sc were corrected for a polyatomic interference with $^{29}Si^{16}O$ following Jenner & O'Neill (2012). This correction assumes that the production of $^{29}Si^{16}O$ is proportional to SiO_2 (in cg g^{-1}) in both sample and standard, and ignores matrix effects. Then, $[Sc]_{sample} = [Sc\#]_{sample} \times [1 + ([SiO_2]_{std.}/[Sc]_{std.}) \times 0·0128] - 0·0128 \times [SiO_2]_{sample}$; where $[Sc\#]_{sample}$ is the apparent Sc (in μg g^{-1}) determined on the sample, and the value of 0·0128 is the interference production rate, which was determined on San Carlos olivine using a Finnigan MAT Neptune mass spectrometer by S. M. Eggins (personal communication). Although the absolute concentrations of trace elements determined by LA-ICP-MS may be affected by several factors (see Jenner & O'Neill, 2012), most of the systematic error, including the uncertainties in the standards, cancels out during the calculation of crystal/melt partition coefficients.

RESULTS

In total, our experimental work produced 37 'daughter' compositions: seven DFA + Fa–FeO, seven DFA + Al_2O_3, seven DFA + Al_2O_3 + Na, seven MORB-ol + $Fo_{100–40}$, seven MORB-ol + $Fo_{100–40}$ + Na, one M666, and one M666 + K (Tables 1 and 2). Some samples were lost by falling prematurely or sticking together during the course of the 1 bar experiments, hence the gaps in the dataset. All compositions upon quenching produced euhedral to subhedral olivine crystals (ranging from Fo_{100} to Fo_{60}) with a few up to ~100 μm across and clear silicate glass, except for the two highest Fe samples in run B05/04/11 (#6 and #7), which formed a microcrystalline matrix upon quenching. Occasionally, some compositions crystallized small amounts of pyroxenes and/or spinel, but the chemical compositions of these mineral phases are not reported here.

Major element analyses of silicate melts and olivines are presented in Supplementary Data Electronic Appendices 1 and 2, respectively (available for downloading at http://www.petrology.oxfordjournals.org). We did not analyze the major element composition of olivines produced from Fe-free experiments (C04/04/11, B28/03/11, B21/03/11, D1264, C4240, C4234 and C4241) as this phase must be nearly pure forsterite. Trace element concentrations of silicate melts and olivines are presented in Electronic Appendices 3 and 4, respectively. The major and trace element concentrations of the melt phase in samples #6 and #7 from run B05/04/11, which formed a microcrystalline matrix upon quenching, show greater variability. Accordingly, we have obtained a large number of single analyses in these samples covering a much larger area than for other experiments, so that average values would be representative of the original melt composition at high temperature. Olivine crystals are usually fairly homogeneous in major (i.e. Fe/Mg) elements, as illustrated by the uncertainties determined on replicate measurements given in Electronic Appendix 2. For MgO and FeO, for instance, 1σ uncertainty in olivine determinations on single samples is typically below 1% and 2%, respectively. Trace elements in olivine are also mostly homogeneous (Electronic Appendix 4), with the exception of olivines crystallizing from both Fe- and Al-rich compositions at lower temperature. For these samples, we observe zoning of Al, which is highly correlated with zoning of other trivalent cations (e.g. Cr, V, Sc, Y and the REE). We suspect the reason for this may be that olivine initially crystallized metastably with high Al, which then diffuses too slowly to re-equilibrate before crystal growth. For these samples, a larger than usual number of measurements were carried out, and only the determinations with the lowest Al contents in olivine were considered. Olivine/silicate melt partitioning coefficients for Na, Al, Ca, Sc, Ti, V, Cr, Mn, Y, Zr, Tb, Er and Yb, calculated using the LA-ICP-MS data given in Electronic Appendices 3 and 4, are presented in Table 3.

DISCUSSION

Calibration of V olivine/melt partitioning as an oxybarometer

Vanadium is a multivalent element that may occur in natural systems, in addition to its metallic form, as V^{2+}, V^{3+}, V^{4+} and V^{5+}. Previous experimental studies have quantified the changes in bulk V olivine/melt partitioning ($D_V^{ol/melt}$) as a function of oxygen fugacity (Canil, 1997; Canil & Fedortchouk, 2001; Shearer *et al.*, 2006;

Table 3: Olivine/silicate–melt partition coefficients

Experiments	*D*(Na)	*D*(Al)	*D*(Ca)	*D*(Sc)	*D*(Ti)	*D*(V)	*D*(Cr)	*D*(Mn)	*D*(Y)	*D*(Zr)	*D*(Tb)	*D*(Er)	*D*(Yb)
DFA compositions													
B05/04/11-1	—	—	0·0390 (015)	0·0794 (024)	—	0·0091 (003)	—	0·707 (013)	0·00506 (014)	0·00040 (013)	0·00185 (005)	0·0067 (002)	0·0131 (004)
B05/04/11-2	—	—	0·0314 (009)	0·0732 (031)	—	0·0109 (005)	—	0·678 (013)	0·00412 (014)	0·00039 (008)	0·00151 (010)	0·0056 (002)	0·0112 (004)
B05/04/11-3	—	—	0·0292 (010)	0·0777 (019)	—	0·0120 (006)	—	0·668 (010)	0·00422 (011)	0·00056 (036)	0·00157 (007)	0·0058 (001)	0·0116 (003)
B05/04/11-4	—	—	0·0303 (013)	0·0817 (031)	—	0·0121 (004)	0·369 (022)	0·677 (014)	0·00459 (016)	0·00045 (014)	0·00167 (007)	0·0063 (002)	0·0123 (004)
B05/04/11-5	—	—	0·0276 (011)	0·0679 (021)	—	0·0121 (004)	0·641 (206)	0·648 (014)	0·00359 (015)	0·00044 (016)	0·00131 (009)	0·0049 (002)	0·0097 (004)
B05/04/11-6	—	—	0·0428 (010)	0·0789 (013)	—	0·0070 (003)	0·288 (050)	0·706 (009)	0·00521 (010)	0·00033 (005)	0·00195 (005)	0·0073 (002)	0·0141 (004)
B05/04/11-7	—	—	0·0650 (021)	0·0835 (032)	—	0·0062 (004)	0·207 (064)	0·692 (019)	0·00764 (037)	0·00024 (010)	0·00276 (019)	0·0097 (004)	0·0185 (008)
C04/04/11-1	0·00288 (024)	0·00387 (056)	0·0476 (046)	0·2786 (228)	—	0·0594 (019)	0·754 (213)	0·846 (026)	0·01964 (272)	0·00099 (101)	0·00733 (116)	0·0258 (036)	0·0492 (068)
C04/04/11-2	0·00285 (023)	0·00305 (019)	0·0475 (035)	0·2627 (083)	—	0·0644 (033)	1·392 (296)	0·823 (023)	0·01833 (069)	0·00071 (037)	0·00684 (035)	0·0244 (011)	0·0469 (019)
C04/04/11-3	0·00286 (038)	0·00602 (032)	0·0520 (025)	0·3981 (152)	—	0·0703 (027)	1·385 (343)	0·888 (015)	0·03033 (117)	0·00154 (078)	0·01094 (039)	0·0398 (016)	0·0762 (033)
C04/04/11-4	0·00363 (142)	0·00795 (045)	0·0522 (025)	0·4927 (200)	—	0·0872 (031)	1·163 (286)	0·933 (015)	0·03717 (180)	0·00197 (031)	0·01345 (071)	0·0491 (024)	0·0949 (037)
C04/04/11-5	0·00292 (041)	—	0·0440 (029)	0·2660 (087)	—	0·0752 (034)	0·840 (140)	0·774 (023)	0·01832 (126)	0·00088 (059)	0·00690 (043)	0·0244 (019)	0·0469 (036)
C04/04/11-6	0·00316 (040)	0·00327 (023)	0·0478 (043)	0·2703 (102)	—	0·0621 (017)	0·849 (166)	0·822 (030)	0·01973 (128)	—	0·00714 (037)	0·0261 (019)	0·0501 (041)
C04/04/11-7	0·00334 (069)	0·00519 (056)	0·0519 (021)	0·3311 (065)	—	0·0692 (018)	1·113 (155)	0·947 (032)	0·02515 (084)	0·00171 (093)	0·00923 (040)	0·0333 (007)	0·0642 (025)
B28/03/11-1	—	0·00527 (019)	0·0265 (011)	0·1597 (045)	—	0·0324 (011)	—	0·709 (013)	0·00858 (032)	0·00051 (014)	0·00304 (014)	0·0117 (006)	0·0235 (009)
B28/03/11-2	—	0·00408 (025)	0·0268 (014)	0·1255 (045)	—	0·0268 (010)	—	0·706 (014)	0·00679 (027)	0·00043 (013)	0·00244 (015)	0·0093 (004)	0·0188 (008)
B28/03/11-3	—	0·00254 (017)	0·0281 (006)	0·0805 (013)	—	0·0211 (008)	—	0·662 (007)	0·00429 (010)	0·00035 (015)	0·00155 (004)	0·0059 (001)	0·0119 (002)
B28/03/11-4	—	0·00669 (021)	0·0246 (014)	0·1897 (051)	—	0·0378 (012)	—	0·697 (016)	0·01006 (032)	0·00063 (014)	0·00353 (014)	0·0137 (004)	0·0278 (009)
B28/03/11-5	—	0·00314 (017)	0·0276 (012)	0·1011 (040)	—	0·0234 (009)	—	0·692 (011)	0·00546 (020)	0·00042 (012)	0·00197 (005)	0·0076 (003)	0·0151 (005)
B28/03/11-6	—	0·00290 (015)	0·0276 (009)	0·0922 (026)	—	0·0228 (010)	—	0·689 (007)	0·00500 (018)	0·00035 (009)	0·00179 (005)	0·0069 (003)	0·0137 (004)
B28/03/11-7	—	—	0·0282 (014)	0·0700 (025)	—	0·0214 (006)	—	0·635 (008)	0·00365 (016)	0·00029 (004)	0·00132 (004)	0·0050 (002)	0·0101 (004)
B21/03/11-1	—	0·00303 (025)	0·0257 (016)	0·0953 (074)	—	0·0808 (017)	0·854 (096)	0·695 (016)	0·00511 (041)	0·00038 (008)	0·00183 (014)	0·0071 (006)	0·0141 (012)
B21/03/11-2	—	0·00289 (030)	0·0284 (007)	0·0911 (028)	—	0·0768 (020)	0·576 (147)	0·679 (010)	0·00489 (017)	0·00034 (010)	0·00177 (009)	0·0067 (003)	0·0134 (005)
B21/03/11-3	—	0·00414 (035)	0·0272 (009)	0·1243 (071)	—	0·0902 (032)	0·751 (235)	0·719 (024)	0·00671 (043)	0·00039 (014)	0·00241 (018)	0·0092 (007)	0·0186 (013)
B21/03/11-4	—	—	0·0256 (022)	0·0643 (056)	—	0·0729 (037)	—	0·630 (021)	0·00338 (031)	0·00042 (022)	0·00128 (015)	0·0046 (004)	0·0091 (009)
B21/03/11-5	—	0·00259 (013)	0·0280 (007)	0·0807 (022)	—	0·0731 (016)	—	0·657 (017)	0·00434 (015)	0·00037 (007)	0·00156 (010)	0·0059 (003)	0·0117 (005)
B21/03/11-6	—	0·00550 (045)	0·0254 (018)	0·1581 (125)	—	0·1070 (053)	0·753 (270)	0·709 (012)	0·00841 (079)	0·00052 (009)	0·00300 (029)	0·0115 (008)	0·0233 (020)
B21/03/11-7	—	0·00645 (030)	0·0247 (013)	0·1814 (064)	—	0·1146 (040)	0·951 (342)	0·687 (018)	0·00969 (037)	0·00063 (011)	0·00340 (017)	0·0132 (005)	0·0268 (010)

(continued)

Table 3: Continued

Experiments	*D*(Na)	*D*(Al)	*D*(Ca)	*D*(Sc)	*D*(Ti)	*D*(V)	*D*(Cr)	*D*(Mn)	*D*(Y)	*D*(Zr)	*D*(Tb)	*D*(Er)	*D*(Yb)
MORB-ol compositions													
B27/01/11-1	–	0·00418 (039)	0·0202 (004)	0·2006 (063)	0·00855 (123)	0·0177 (006)	1·282 (066)	1·220 (040)	0·00553 (019)	0·00065 (027)	0·00161 (012)	0·0081 (005)	0·0184 (009)
B27/01/11-2	–	0·00581 (058)	0·0277 (028)	0·1940 (195)	0·00827 (083)	0·0221 (022)	0·543 (055)	1·065 (107)	0·00739 (074)	0·00075 (008)	0·00262 (027)	0·0105 (011)	0·0241 (024)
B27/01/11-4	–	0·00442 (047)	0·0211 (007)	0·1972 (111)	0·00732 (098)	0·0159 (009)	0·987 (078)	1·157 (025)	0·00614 (038)	0·00069 (028)	0·00187 (015)	0·0090 (007)	0·0203 (010)
B16/01/11-1	–	0·00282 (043)	0·0181 (018)	0·1673 (109)	0·00711 (239)	0·1869 (184)	0·941 (046)	1·020 (007)	0·00526 (056)	0·00031 (003)	0·00162 (021)	0·0080 (009)	0·0171 (009)
B16/01/11-2	–	0·00332 (057)	0·0167 (016)	0·1792 (173)	0·00948 (272)	0·2354 (228)	1·031 (065)	1·046 (024)	0·00485 (047)	0·00057 (033)	0·00145 (009)	0·0073 (008)	0·0162 (014)
B16/01/11-3	–	0·00317 (030)	0·0228 (009)	0·1746 (101)	0·01154 (277)	0·1831 (269)	0·856 (023)	1·013 (008)	0·00652 (038)	0·00062 (007)	0·00214 (019)	0·0093 (007)	0·0202 (014)
B16/01/11-4	–	0·00334 (042)	0·0337 (021)	0·2066 (076)	0·00843 (105)	0·1333 (045)	0·752 (030)	1·047 (010)	0·01014 (067)	0·00076 (025)	0·00346 (026)	0·0142 (007)	0·0296 (017)
B04/03/11-1	–	0·00394 (033)	0·0222 (008)	0·1652 (068)	0·00573 (037)	0·0135 (009)	0·838 (033)	1·043 (034)	0·00585 (035)	0·00053 (005)	0·00185 (010)	0·0081 (005)	0·0184 (005)
B04/03/11-2	–	0·00657 (052)	0·0278 (011)	0·1783 (089)	0·00697 (090)	0·0138 (012)	0·623 (079)	0·974 (032)	0·00767 (046)	0·00067 (019)	0·00248 (011)	0·0105 (007)	0·0227 (010)
B04/03/11-3	–	0·00315 (007)	0·0161 (009)	0·1657 (051)	0·00560 (113)	0·0171 (010)	1·346 (132)	1·191 (087)	0·00476 (010)	0·00065 (018)	0·00154 (042)	0·0073 (001)	0·0162 (017)
B04/03/11-4	–	0·00361 (033)	0·0192 (010)	0·1636 (097)	0·00590 (049)	0·0153 (015)	1·007 (064)	1·049 (047)	0·00544 (036)	0·00056 (014)	0·00169 (017)	0·0079 (008)	0·0175 (010)
B04/03/11-5	–	0·00469 (025)	0·0219 (008)	0·1569 (079)	0·00582 (044)	0·0139 (005)	0·769 (080)	1·002 (040)	0·00604 (036)	0·00053 (013)	0·00198 (020)	0·0084 (003)	0·0189 (010)
B04/03/11-6	–	0·00560 (056)	0·0246 (025)	0·1626 (163)	0·00584 (059)	0·0145 (015)	0·660 (067)	0·986 (100)	0·00669 (068)	0·00060 (006)	0·00232 (023)	0·0096 (010)	0·0201 (020)
C15/03/11-1	0·00163 (117)	0·00505 (065)	0·0787 (065)	0·6379 (357)	0·01985 (253)	0·1705 (195)	1·581 (078)	1·110 (029)	0·05891 (394)	0·00958 (353)	0·02118 (149)	0·0794 (058)	0·1552 (116)
C15/03/11-2	0·00119 (050)	0·00407 (044)	0·0550 (038)	0·4250 (338)	0·01307 (107)	0·1461 (128)	1·310 (078)	1·013 (027)	0·03079 (348)	0·00102 (044)	0·01108 (105)	0·0401 (045)	0·0801 (083)
C15/03/11-3	0·00115 (077)	0·00521 (054)	0·0817 (129)	0·5944 (866)	0·01781 (232)	0·1239 (111)	1·299 (127)	1·075 (076)	0·05234 (981)	0·00198 (106)	0·01921 (339)	0·0697 (141)	0·1352 (281)
C15/03/11-4	–	0·00443 (082)	0·0555 (170)	0·4831 (1389)	0·01433 (303)	0·1702 (190)	1·607 (304)	1·104 (057)	0·03743 (1598)	0·00310 (322)	0·01341 (525)	0·0502 (224)	0·0994 (460)
C15/03/11-5	0·00122 (071)	0·00393 (067)	0·0505 (097)	0·3935 (580)	0·01257 (138)	0·1789 (136)	1·493 (145)	1·085 (092)	0·02693 (497)	0·00097 (037)	0·00965 (151)	0·0367 (068)	0·0723 (147)
C15/03/11-6	0·00193 (046)	0·00586 (049)	0·0939 (042)	0·6530 (447)	0·02009 (240)	0·1116 (294)	1·264 (085)	1·070 (042)	0·06168 (518)	0·00236 (158)	0·02234 (178)	0·0822 (078)	0·1555 (159)
C15/03/11-7	0·00122 (038)	0·00415 (041)	0·0423 (069)	0·3399 (533)	0·01218 (119)	0·2538 (629)	1·940 (464)	1·122 (080)	0·02135 (474)	0·00096 (060)	0·00779 (175)	0·0284 (061)	0·0572 (121)
C10/03/11-1	0·00215 (132)	0·00327 (054)	0·0524 (120)	0·3285 (399)	0·00879 (130)	0·0187 (023)	1·773 (207)	1·240 (066)	0·01812 (361)	0·00058 (056)	0·00618 (108)	0·0246 (048)	0·0503 (096)
C10/03/11-2	0·00269 (165)	0·00353 (069)	0·0494 (098)	0·3201 (312)	0·00914 (106)	0·0183 (040)	1·617 (087)	1·214 (030)	0·01779 (308)	0·00062 (048)	0·00634 (101)	0·0240 (038)	0·0482 (061)
C10/03/11-3	0·00190 (125)	0·00356 (063)	0·0386 (087)	0·3246 (359)	0·00802 (066)	0·0232 (030)	1·757 (284)	1·226 (025)	0·01512 (339)	0·00107 (093)	0·00535 (108)	0·0210 (047)	0·0434 (098)
C10/03/11-4	0·00094 (053)	0·00319 (034)	0·0425 (171)	0·2895 (386)	0·00795 (169)	0·0198 (036)	1·374 (258)	1·157 (049)	0·01461 (387)	0·00046 (022)	0·00501 (125)	0·0199 (055)	0·0415 (101)
C10/03/11-5	0·00281 (030)	0·00550 (027)	0·0796 (043)	0·3913 (189)	0·01284 (123)	0·0136 (031)	1·777 (418)	1·067 (035)	0·02894 (198)	0·00083 (041)	0·01032 (103)	0·0383 (027)	0·0767 (054)
C10/03/11-6	0·00218 (019)	0·00381 (058)	0·0492 (061)	0·3018 (244)	0·01046 (167)	0·0180 (032)	1·568 (146)	1·170 (050)	0·01704 (232)	0·00118 (063)	0·00595 (088)	0·0235 (037)	0·0472 (055)
C10/03/11-7	0·00351 (053)	0·00490 (062)	0·0588 (134)	0·3110 (489)	0·01111 (204)	0·0169 (025)	1·447 (110)	1·137 (045)	0·02000 (552)	0·00083 (056)	0·00720 (198)	0·0269 (075)	0·0537 (148)
C12/01/11-1	–	0·00502 (031)	0·0273 (012)	0·1919 (046)	0·01039 (176)	0·0444 (058)	0·746 (029)	0·959 (008)	0·00824 (025)	0·00079 (017)	0·00276 (010)	0·0116 (005)	0·0248 (006)
C12/01/11-2	–	0·00465 (018)	0·0205 (007)	0·2054 (119)	0·01018 (051)	0·0691 (137)	1·253 (042)	1·009 (019)	0·00631 (048)	0·00068 (022)	0·00193 (010)	0·0093 (004)	0·0213 (014)
C12/01/11-3	–	0·00309 (007)	0·0173 (015)	0·1661 (045)	0·00639 (062)	0·0449 (013)	1·034 (023)	0·976 (034)	0·00487 (012)	0·00048 (009)	0·00147 (013)	0·0070 (001)	0·0160 (007)

(continued)

Table 3: Continued

Experiments	*D*(Na)	*D*(Al)	*D*(Ca)	*D*(Sc)	*D*(Ti)	*D*(V)	*D*(Cr)	*D*(Mn)	*D*(Y)	*D*(Zr)	*D*(Tb)	*D*(Er)	*D*(Yb)
C12/01/11-4	—	0·00366 (016)	0·0218 (006)	0·1764 (055)	0·00763 (090)	0·0415 (024)	0·883 (022)	0·982 (009)	0·00630 (018)	0·00054 (016)	0·00196 (011)	0·0090 (004)	0·0198 (009)
B19/02/11-1	—	0·00387 (033)	0·0217 (013)	0·1647 (116)	0·00759 (090)	0·1401 (082)	0·773 (040)	0·824 (014)	0·00672 (055)	0·00065 (019)	0·00220 (017)	0·0097 (008)	0·0202 (015)
B19/02/11-2	—	0·00487 (085)	0·0181 (006)	0·1867 (137)	0·01001 (172)	0·1835 (120)	0·920 (054)	0·821 (024)	0·00640 (064)	0·00144 (108)	0·00213 (043)	0·0092 (008)	0·0200 (013)
B19/02/11-3	—	0·00368 (042)	0·0206 (007)	0·1661 (103)	0·00749 (110)	0·1505 (067)	0·797 (038)	0·841 (017)	0·00632 (037)	0·00069 (033)	0·00207 (011)	0·0091 (006)	0·0189 (015)
B19/02/11-4	—	0·00387 (100)	0·0169 (013)	0·1559 (095)	0·00754 (173)	0·1751 (073)	0·906 (067)	0·887 (021)	0·00518 (045)	0·00063 (041)	0·00184 (041)	0·0076 (005)	0·0166 (012)
B15/03/11-1	—	0·00312 (027)	0·0169 (008)	0·1408 (074)	0·00614 (099)	0·1690 (104)	0·913 (026)	0·904 (007)	0·00486 (021)	0·00046 (009)	0·00167 (008)	0·0071 (003)	0·0156 (010)
B15/03/11-3	—	0·00379 (021)	0·0224 (008)	0·1676 (050)	0·00798 (046)	0·1403 (018)	0·794 (023)	0·856 (012)	0·00727 (025)	0·00054 (006)	0·00243 (011)	0·0102 (002)	0·0216 (009)
B15/03/11-4	—	0·00426 (022)	0·0293 (009)	0·1785 (041)	0·00811 (049)	0·1167 (026)	0·703 (017)	0·867 (024)	0·00943 (039)	0·00060 (014)	0·00321 (015)	0·0129 (006)	0·0263 (012)
B15/03/11-5	—	0·00419 (048)	0·0252 (009)	0·1792 (114)	0·00881 (146)	0·1387 (064)	0·810 (035)	0·892 (018)	0·00845 (052)	0·00124 (082)	0·00284 (022)	0·0119 (009)	0·0249 (017)
Komatiite (M666) compositions													
C09/07/09	0·00577 (145)	0·00681 (030)	0·0628 (023)	0·1689 (068)	0·00876 (059)	0·0264 (014)	0·719 (026)	0·915 (019)	0·01419 (051)	0·00045 (015)	0·00527 (021)	0·0187 (009)	0·0354 (015)
C13/07/09	0·01229 (298)	0·00856 (051)	0·0558 (027)	0·1707 (096)	0·00950 (084)	0·0298 (018)	0·746 (044)	0·814 (021)	0·01463 (081)	0·00047 (015)	0·00553 (035)	0·0194 (012)	0·0359 (021)
C09/08/09	—	0·01008 (052)	0·0296 (023)	0·1341 (060)	0·00825 (076)	0·0551 (017)	0·485 (011)	0·591 (010)	0·00863 (046)	0·00086 (023)	0·00332 (024)	0·0115 (006)	0·0222 (012)
C16/07/09	—	0·01198 (052)	0·0484 (016)	0·1634 (081)	0·01054 (048)	0·0354 (031)	0·675 (020)	0·644 (015)	0·01409 (065)	—	0·00548 (035)	0·0185 (005)	0·0343 (023)
C28/07/09A	—	0·01261 (068)	0·0321 (026)	0·1355 (061)	0·01004 (075)	0·0540 (029)	0·495 (021)	0·598 (046)	0·00998 (039)	0·00105 (025)	0·00394 (019)	0·0132 (009)	0·0256 (013)
C28/07/09B	—	0·01125 (071)	0·0317 (014)	0·1298 (052)	0·00890 (113)	0·0483 (028)	0·449 (014)	0·555 (009)	0·00964 (032)	0·00095 (031)	0·00383 (026)	0·0129 (005)	0·0239 (009)
C07/08/09	0·01629 (544)	0·01033 (082)	0·0314 (027)	0·1428 (107)	0·00994 (146)	0·0956 (045)	0·471 (015)	0·552 (010)	0·01078 (107)	0·00086 (042)	0·00431 (055)	0·0141 (014)	0·0267 (024)
C08/08/09	—	0·01493 (062)	0·0349 (034)	0·1536 (064)	0·01041 (091)	0·0217 (014)	0·460 (027)	0·624 (017)	0·01113 (074)	0·00075 (024)	0·00430 (018)	0·0144 (015)	0·0275 (010)
B16/09/09	—	0·01091 (093)	0·0326 (025)	0·1303 (048)	0·00950 (089)	0·0628 (032)	0·462 (007)	0·558 (008)	0·01025 (075)	0·00125 (053)	0·00428 (048)	0·0132 (009)	0·0245 (010)
C05/02/10	—	0·00888 (050)	0·0230 (016)	0·1321 (036)	0·00595 (047)	0·0046 (004)	0·510 (094)	0·677 (009)	0·00603 (034)	0·00071 (022)	0·00216 (033)	0·0081 (004)	0·0171 (007)
C15/01/10	—	0·00984 (046)	0·0243 (012)	0·1339 (044)	0·00637 (053)	0·0048 (002)	0·463 (016)	0·642 (015)	0·00651 (024)	0·00070 (013)	0·00227 (013)	0·0090 (004)	0·0184 (011)
C19/01/10	—	0·01116 (041)	0·0248 (017)	0·1395 (037)	0·00754 (058)	0·0062 (002)	0·545 (031)	0·612 (012)	0·00742 (021)	0·00067 (017)	0·00271 (012)	0·0101 (004)	0·0203 (007)
C22/01/10	—	0·01274 (124)	0·0281 (012)	0·1500 (077)	0·00925 (112)	0·0083 (013)	0·559 (060)	0·564 (005)	0·00926 (064)	0·00091 (034)	0·00352 (042)	0·0122 (010)	0·0240 (018)
High-pressure experiments													
C4036	—	0·00484 (029)	0·0160 (049)	0·1181 (061)	0·00399 (082)	0·0030 (002)	0·484 (069)	0·771 (020)	0·00372 (044)	—	0·00110 (021)	0·0054 (004)	0·0116 (009)
C4033	—	0·00838 (184)	0·0174 (021)	0·1032 (067)	0·00566 (103)	0·0036 (005)	0·735 (310)	0·661 (009)	0·00383 (018)	0·00066 (021)	0·00125 (012)	0·0054 (007)	0·0115 (009)
C4038	—	0·01010 (271)	0·0173 (028)	0·1192 (066)	0·00617 (254)	0·0039 (005)	0·430 (036)	0·642 (014)	0·00520 (025)	—	0·00179 (042)	0·0071 (005)	0·0148 (014)
D1264	—	0·00950 (061)	0·0221 (015)	0·1099 (049)	0·00729 (031)	—	—	—	0·00447 (026)	0·00055 (010)	—	—	—
C4240	—	0·00651 (029)	0·0224 (009)	0·1582 (059)	0·00593 (034)	0·0273 (019)	0·678 (015)	0·635 (012)	0·00852 (039)	0·00063 (020)	0·00307 (020)	0·0116 (007)	0·0227 (011)
C4234	—	0·00827 (056)	0·0211 (020)	0·1649 (051)	0·00621 (084)	0·0648 (025)	—	0·689 (021)	0·00775 (042)	0·00081 (022)	0·00287 (030)	0·0104 (004)	0·0205 (007)
C4241	—	0·00767 (032)	0·0167 (010)	0·1272 (041)	0·00473 (036)	0·0531 (018)	0·618 (016)	0·655 (011)	0·00464 (023)	0·00065 (031)	0·00164 (012)	0·0065 (002)	0·0132 (005)

Uncertainties (1σ standard deviation) are given in parenthesis for the last significant figures.

Mallmann & O'Neill, 2009). The results, which are illustrated in Fig. 1, indicate that V becomes progressively more incompatible in olivine with increasing valence state (i.e. $D_{V^{2+}}^{ol/melt} > D_{V^{3+}}^{ol/melt} > D_{V^{4+}}^{ol/melt} > D_{V^{5+}}^{ol/melt}$), as imposed by changes in oxygen fugacity. In going from all V^{2+} (compatible) to all V^{5+} (highly incompatible), $D_V^{ol/melt}$ changes by four orders of magnitude over about 20 orders of magnitude in oxygen fugacity. Although the results for sets of experiments where the only effective variable is oxygen fugacity can be described well by a rigorous equation derived from the thermodynamic description of the partitioning equilibria, the equation involves seven parameters: four partition coefficients (one for each of the V valence states) and three equilibrium constants relating the changes in V valence states [see Mallmann & O'Neill, 2009; their equation (15)]. Each of these seven parameters is expected to vary with temperature and pressure, potentially with different sensitivities to these variables. Moreover, each of the four partition coefficients is expected to vary with melt composition, again often in different ways for each V valence state. Although the variation observed in $D_V^{ol/melt}$ owing to differences in composition and/or temperature is small compared with the variation with oxygen fugacity (Fig. 1), it is easily discernible in the results of Mallmann & O'Neill (2009) by comparing their data on different compositions (e.g. V1 and V8 versus V5 and V7; see their fig. 3a). Not addressed by the experiments of Mallmann & O'Neill (2009) is the further possibility that the four partition coefficients also vary with olivine composition (i.e. Mg/Fe ratio), potentially also in different ways. Empirically, the values of $D_V^{ol/melt}$ shown in Fig. 1 suggest that $D_V^{ol/melt}$ may vary by approximately a factor of four at equivalent oxygen fugacities.

We therefore feel that a thermodynamically based calibration of V olivine/melt partitioning as an oxybarometer would be prohibitively tedious, and we have instead chosen to parameterize the variation of $D_V^{ol/melt}$ with oxygen fugacity empirically. For convenience, we will consider only experiments performed at oxygen fugacities between QFM−4 and QFM+4 [i.e. between four $\log_{10}$ units more reduced or oxidized than the quartz–fayalite–magnetite (QFM) equilibria at specific temperature], over which range the variation of $D_V^{ol/melt}$ with oxygen fugacity on a logarithm scale is nearly linear (Fig. 1). It should be noted that most geological planetary processes also occur over this range of oxygen fugacity conditions. Our target

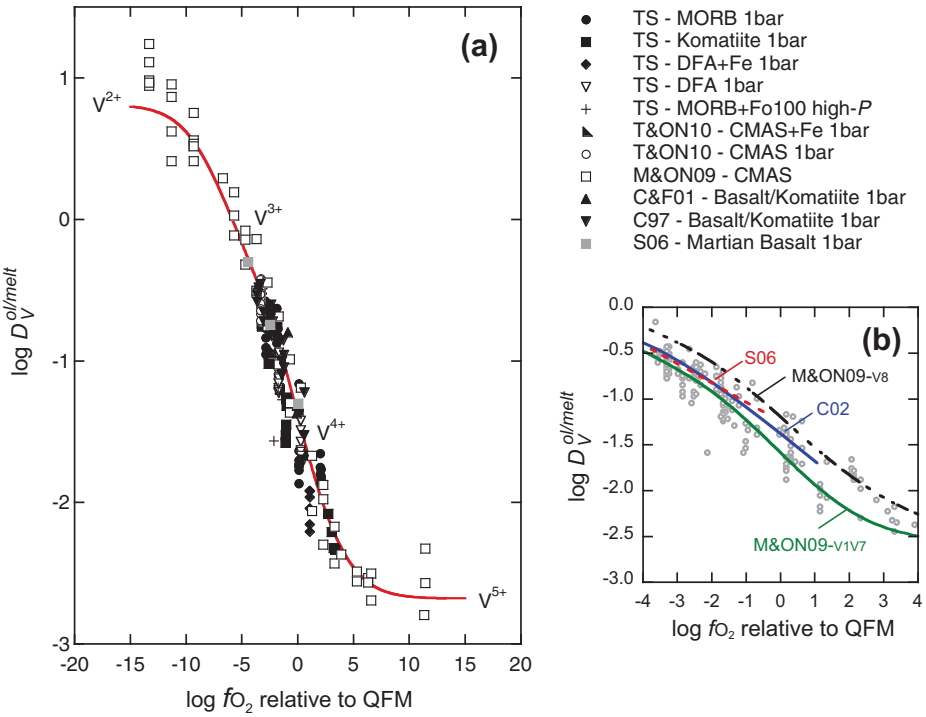

Fig. 1. The effect of oxygen fugacity on the partitioning of vanadium between olivine and silicate melt. Oxygen fugacity is given in customary $\log_{10}$ units relative to the quartz–fayalite–magnetite (QFM) buffer (O'Neill, 1987). (a) Available experimental data: C97, Canil (1997); C&F01, Canil & Fedortchouk (2001); C02, Canil (2002); S06, Shearer *et al.* (2006); M&ON09, Mallmann & O'Neill (2009); T&ON10, Tuff & O'Neill (2010); TS, this study. The continuous line represents the regression of the entire dataset to equation (15) of Mallmann & O'Neill (2009). (b) Detail of previous calibrations relating the partitioning of V between olivine and silicate melt with oxygen fugacity (plot restricted between QFM−4 and QFM+4). The experimental data are plotted in the background (grey circles) for reference. It should be noted that none of these calibrations account for variable temperature, pressure and/or olivine and melt composition as each has been constrained for a particular set of conditions.

was to find an expression that could fit the experimental data to within its analytical accuracy. With this kind of approach there is always the problem that an aberrant datum or two (and such are not unknown in large experimental datasets) may demand an extra parameter to give a statistically good fit, particularly if the aberrant data are near the extremes of the compositional space of the dataset. The whole fit is then biased by this parameter. We have therefore chosen to err on the side of using as few parameters as possible. After performing stepwise regressions including all possible major-element melt composition parameters and eliminating those that returned insignificant figures (i.e. within two standard deviations of zero), we arrived to the following expression:

$$\begin{aligned}\log_{10} D_{\mathrm{V}}^{\mathrm{ol/melt}} &= a_0 + a_1(\Delta\mathrm{NNO/QFM}) + a_2/T \\ &+ a_3(1-\mathrm{Mg}_{\#}^{\mathrm{ol}})^2/T + a_4 X_{\mathrm{KO}_{0.5}}^{\mathrm{melt}}/T \\ &+ a_5(X_{\mathrm{CaO}}^{\mathrm{melt}} + X_{\mathrm{NaO}_{0.5}}^{\mathrm{melt}})/T \\ &+ a_6(X_{\mathrm{SiO}_2}^{\mathrm{melt}} + X_{\mathrm{AlO}_{1.5}}^{\mathrm{melt}})/T\end{aligned} \quad (1)$$

where ΔNNO/QFM refers to oxygen fugacity (in customary $\log_{10}$ units) relative to oxygen buffers, either Ni–NiO (NNO) or quartz–fayalite–magnetite (QFM), and T is in Kelvin. We define mole fractions in the melt on the single-cation basis (see Tuff & O'Neill, 2010). The result for the regression, which was weighted considering only the uncertainties in $D_{\mathrm{V}}^{\mathrm{ol/melt}}$ (1σ standard deviation as observed or 3%, whichever is larger), is presented in Table 4. Fourteen aberrant data points, listed in Table 4, were rejected as outliers. These data fall more than two standard deviations away from calculated values, even if additional terms are introduced to the model. The reduced chi-squared (χ^2_{v}) statistic of the fit to the remaining 175 data is 2·8, which indicates that the model is a fair representation of the data, considering that the uncertainties in all the other parameters were not included. We also tried

Table 4: Best-fit parameters obtained by least-squares regression of experimental data to equations (1) and (2)

Parameter	Equation (1) log fO_2 as ΔQFM	Equation (1) log fO_2 as ΔNNO	Parameter	Equation (2) T in K, P in GPa
a0	−2·032 ± 0·109	−1·845 ± 0·108	b0	−1·471 ± 0·066
a1	−0·2639 ± 0·0013	−0·2635 ± 0·0013	b1	3230 ± 110
a2	−822 ± 252	−1372 ± 252	b2	100 ± 22
a3	3328 ± 361	3389 ± 361	b3	1402 ± 58
a4	−5326 ± 304	−5318 ± 304	b4	−1933 ± 78
a5	−746 ± 98	−747 ± 98	b5	−2612 ± 111
a6	3254 ± 129	3259 ± 129	b6	569 ± 104
n	175	175	n	186
χ^2_{v}	2·77	2·78	χ^2_{v}	0·49

Regressions were performed using the non-linear least-squares Levenberg–Marquardt algorithm. Rejected data [equation (1)]: B16/01/11-4, C15/03/11-7, C04/04/11-5, B05/04/11-6, B05/04/11-7, C04/04/11-5, C19/01/10, C22/01/10 (this study); N89B3 (Tuff & O'Neill, 2010); V1300-5 (Mallmann & O'Neill, 2009); 135auk1 (Canil & Fedortchouk, 2001); 22komv, 50hss, 21komv (Canil, 1997). Rejected data [equation (2)]: C15/03/11-1, C10/03/11-3 (this study); CMAS N81B2, CMAS N81B3 (Tuff & O'Neill, 2010); CMAS-Foe (Evans *et al.*, 2008); V1300-10 V7, V1300-13 V5 (Mallmann & O'Neill, 2009).

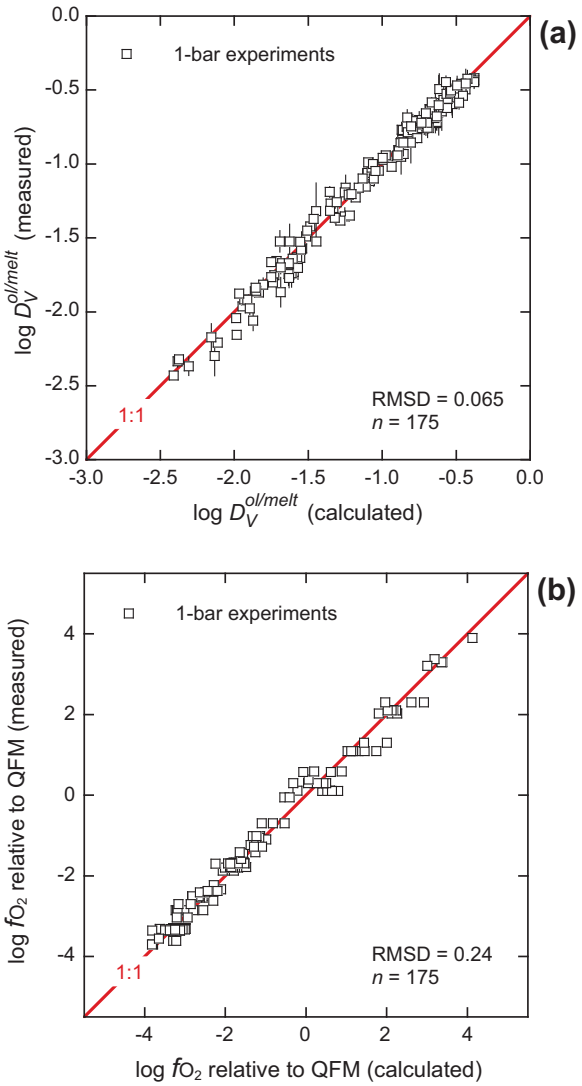

Fig. 2. (a) Comparison between the $D_{\mathrm{V}}^{\mathrm{ol/melt}}$ measured in 175 experiments (Canil, 1997; Canil & Fedortchouk, 2001; Mallmann & O'Neill, 2009; Tuff & O'Neill, 2010; this study) and calculated from equation (1) with coefficients given in Table 4. Error bars are 1σ standard deviation as measured or 3%, whichever is larger. (b) Comparison between the oxygen fugacity of experiments (measured) and those calculated from $D_{\mathrm{V}}^{\mathrm{ol/melt}}$ using equation (1) with coefficients given in Table 4.

to regress the data with mole fractions of oxide metals in the melt as entropy-like terms (i.e. term not divided by temperature), but a better fit was always achieved when they were treated as enthalpy-like terms. Figure 2a illustrates the results of the fit by plotting calculated versus measured $D_V^{ol/melt}$.

In Fig. 2b we compare oxygen fugacity relative to the QFM buffer determined for 1 bar experiments and those calculated from $D_V^{ol/melt}$. The nominal experimental temperatures were used in the calculation. The empirical $D_V^{ol/melt}$ oxybarometer described here has a root mean square deviation (RMSD) of 0·24 $\log_{10}$ units in oxygen fugacity. Considering the typical precision of V determinations in magmatic olivines and silicate melt (as can be envisaged from the error bars shown in Fig. 2a), we expect the precision of this empirical oxybarometer to be normally better than its accuracy.

Equation (1) does not include a pressure term because at present there are no V olivine/melt partitioning data at pressure under controlled oxygen fugacity with sufficient precision. We have conducted three experiments at the GCO oxygen buffer at pressures of 0·5, 1 and 1·5 GPa to evaluate this effect (Table 2). For these specific pressures at 1400°C, the GCO buffer gives relative oxygen fugacities of QFM–1·60, QFM–1·22 and QFM–0·86 (Table 2), respectively. Relative oxygen fugacities calculated from equation (1) with the parameters of Table 4 for these experiments give QFM+0·36, QFM–1·06 and QFM–0·56. Except for the experiment at 0·5 GPa, which appears to be anomalous, the difference between relative oxygen fugacities expected for the buffer and calculated from $D_V^{ol/melt}$ is close to the uncertainty of the oxybarometer. Although more experiments at pressure under controlled oxygen fugacity are required, we conclude that the effect of pressure is sufficiently small that it may be neglected for the main use envisaged for the oxybarometer, which is for magmatic systems crystallizing olivine at low pressure.

Calibration of the Sc/Y olivine/melt exchange as a geothermometer

Application of the V olivine/melt partitioning oxybarometer [equation (1)] requires knowing the temperature. Although this may be estimated from conventional MgO-geothermometers, the ability to measure trace-element partitioning between olivine and silicate melt precisely using LA-ICP-MS suggested to us that we should search our experimental results for an alternative geothermometer based on trace-element partitioning. The

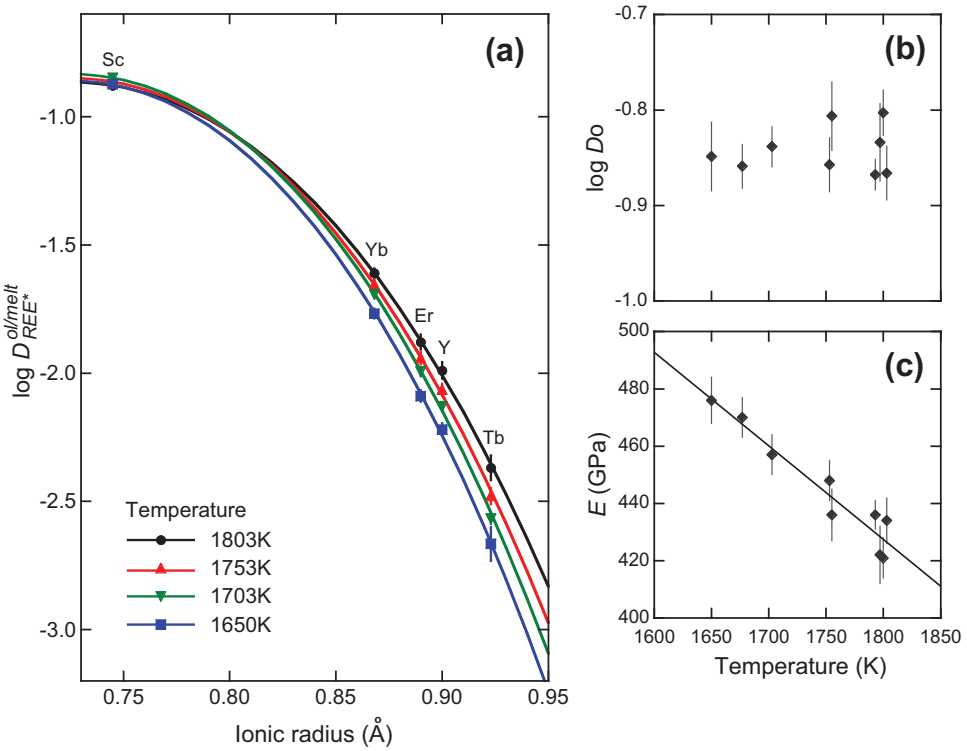

Fig. 3. Partitioning of some heavy rare earth elements plus Sc and Y (REE*) for low-potassium experiments with composition M666 (komatiite) over a range of temperatures. (a) Least-squares fit to the lattice strain model [equation (2) of Blundy & Wood (1994)] for four compositions selected to cover a range of temperatures. Ionic radius in VI-fold coordination taken from Shannon (1976), with assumed uncertainty of 0·002 Å. (b) Experimental temperature versus the parameter D_o (i.e. maximum partition coefficient for the crystal site). Note the lack of correlation. (c) Experimental temperature against the elastic strain parameter of the crystal site (E). Least-squares regression of the data gives: E (GPa) = 994 – 0·324 T (K) (χ^2_ν = 0·77). Errors are one standard deviation and are shown only when larger than symbols.

requirements were good temperature sensitivity but as little sensitivity to melt composition as possible. The latter consideration suggests that an exchange reaction of two trace-element cations with the same substitution mechanisms in olivine would be most suitable, because in such cases the 'stoichiometric control' on each element's substitution into the crystal cancels out (see O'Neill & Eggins, 2002). Also, the trace elements have to be sufficiently abundant in natural magmatic olivines to be measured by LA-ICP-MS precisely, and should not be redox-variable.

We found that the exchange of Sc and Y between olivine and melt ($KD^{ol/melt}_{Sc/Y} = D^{ol/melt}_{Sc}/D^{ol/melt}_{Y}$) fits these criteria fairly well. In Fig. 3 we plot olivine/melt partition coefficients for Sc, Y and other heavy REE obtained for experiments with composition M666 over a range of temperatures. Fitting of these data to the lattice strain model of Blundy & Wood (1994) reveals a strong correlation between the characteristic elastic strain parameter (E) of the crystal site where these trivalent elements substitute and temperature. Similarly, we observe a lack of correlation between E and the mole fraction of SiO_2 in the melt for compositions obtained from the B28/03/11 series at equal temperature (Fig. 4), indicating that the effect of melt composition on $KD^{ol/melt}_{Sc/Y}$ may be limited. In detail, however, there is still a discernible influence of melt and olivine composition on $KD^{ol/melt}_{Sc/Y}$ that becomes evident during data fitting. In the same spirit as used for the calibration of our $D^{ol/melt}_{V}$ oxybarometer, we performed stepwise regressions to eliminate insignificant major-element melt composition parameters and finally arrived to the following expression:

$$\begin{aligned}\log_{10} KD^{ol/melt}_{Sc/Y} = {} & b_0 + b_1/T + b_2P/T \\ & + b_3 Mg^{ol}_{\#}/T + b_4 X^{melt}_{CaO}/T \\ & + b_5(X^{melt}_{NaO_{0.5}} + X^{melt}_{KO_{0.5}})/T \\ & + b_6 X^{melt}_{SiO_2}/T\end{aligned} \quad (2)$$

where T is in Kelvin and P is in GPa. The results of the least-squares regression are summarized in Table 4. Seven aberrant data points, listed in Table 4, were rejected as outliers. Assuming uncertainties in $KD^{ol/melt}_{Sc/Y}$ as measured or 3% (one standard deviation), whichever is larger, the reduced chi-squared (χ^2_ν) statistic of the fit of the remaining 186 data is 0·49. That this value is less than unity may be due to correlation of the analyzed variations between Sc and Y in some samples, owing, for example, to both varying in a systematic way with Al zoning in olivine. As

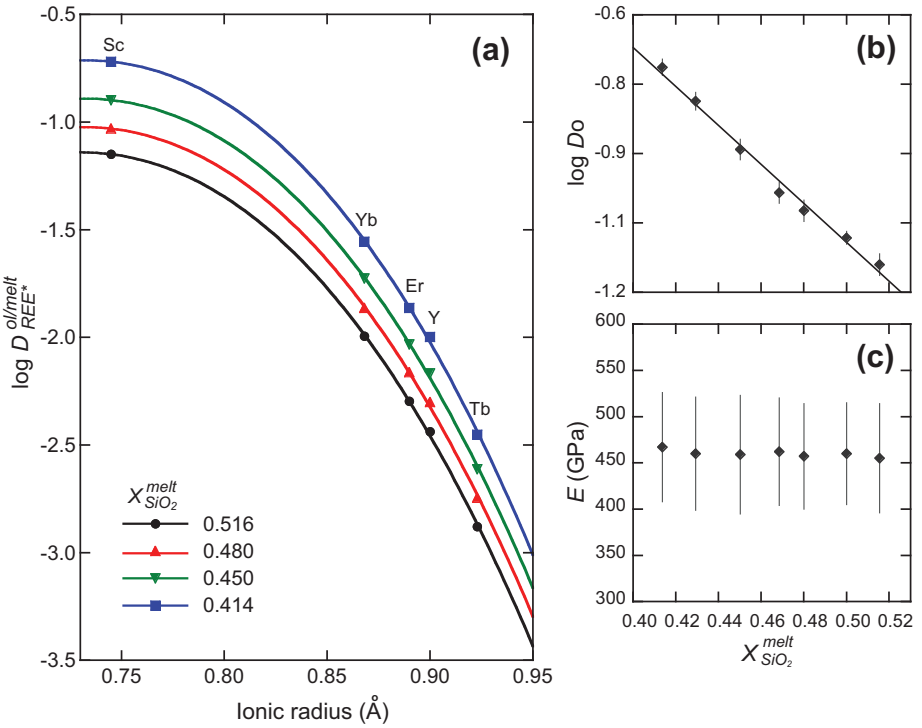

Fig. 4. Partitioning of some heavy rare earth elements plus Sc and Y (REE*) for CMAS compositions from the B28/03/11 series. (a) Least-squares fit to the lattice strain model [equation (2) of Blundy & Wood (1994)] for four compositions selected to cover a range of SiO_2 in the melt. Ionic radius in VI-fold coordination taken from Shannon (1976), with assumed uncertainty of 0·002 Å. (b) Mole fraction of SiO_2 in the melt versus the parameter D_o (i.e. maximum partition coefficient for the crystal site). Least-squares regression of the data gives $\log D_o = 1{\cdot}02 - 4{\cdot}22 X^{melt}_{SiO_2}$ ($\chi^2_\nu = 0{\cdot}91$). (c) Mole fraction of SiO_2 in the melt versus the elastic strain parameter of the crystal site (E). Note the lack of correlation. Errors are one standard deviation and are shown only when larger than symbols.

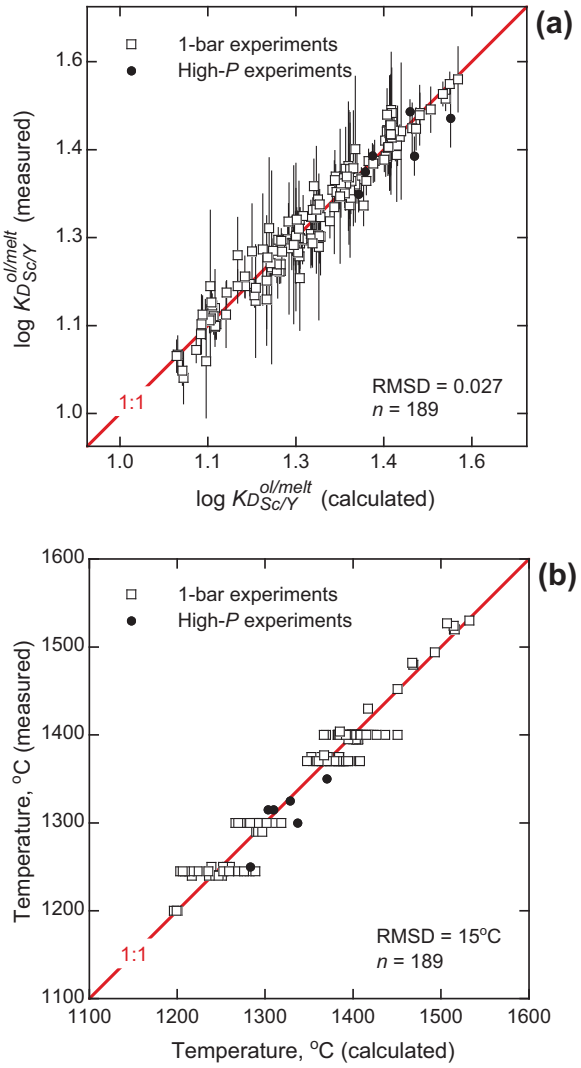

Fig. 5. (a) Comparison between the $KD_{Sc/V}^{ol/melt}$ measured in 189 experiments (Evans *et al.*, 2008; Mallmann & O'Neill, 2009; Tuff & O'Neill, 2010; this study) and calculated from equation (2) with coefficients given in Table 4. Error bars are 1σ standard deviation as measured or 3%, whichever is larger. (b) Comparison between the temperature of experiments (measured) and those calculated from $KD_{Sc/V}^{ol/melt}$ using equation (2) with coefficients given in Table 4.

for the fitting of the $D_V^{ol/melt}$ data, a better fit was always obtained by treating the terms in the mole fractions of the oxide components in the melt as enthalpy-like terms. Figure 5a illustrates the results of the fit by plotting calculated versus measured $KD_{Sc/Y}^{ol/melt}$. To test the validity of equation (2) as a geothermometer, in Fig. 5b we plot calculated versus measured temperatures for the 186 experiments used in the regression, which cover a range of temperature from 1200 to 1530°C. Taking the RMSD as an indication, the accuracy of the $KD_{Sc/Y}^{ol/melt}$ geothermometer is estimated to be about 15°C. The precision, however, will be strongly dependent on the precision of Sc and Y determinations. Potentially, the precision of the $KD_{Sc/Y}^{ol/melt}$ geothermometer could be augmented by also using the partitioning of the REE, which have the same 'stoichiometric control' in their substitution into olivine as Y and Sc. For example, we could envisage a least-squares approach using Y/Sc plus several REE/Sc ratios as the variables. However, at present, using the REE would add little to the precision of the geothermometry because only the heaviest REE are sufficiently compatible in olivine to have abundances measurable by LA-ICP-MS (e.g. Witt-Eickschen & O'Neill, 2005), and the partitioning of the REE relative to Sc becomes less sensitive to temperature with increasing compatibility (Fig. 3).

For comparison, we calculated temperature using various MgO-geothermometers for 66 experiments, filtered from the 186 data used above to exclude experiments at pressure higher than 1 bar, and those rich in alkalis and from Fe-free systems, which are far from the natural compositions at which these geothermometers are aimed (Fig. 6). Two calibrations stand out as performing well, both in terms of accuracy and precision: that of Ford *et al.* (1983) and equation (4) of Putirka *et al.* (2007). However, the RMSD calculated for these geothermometers (using 66 data points and corrected for systematic error) is between 24 and 25°C, hence larger than the value of 15°C obtained for the $KD_{Sc/Y}^{ol/melt}$ geothermometer using the whole dataset of 186 experiments (or 14°C when selecting the same 66 data; Fig. 6f).

APPLICATION

Rearranging equations (1) and (2) and using the coefficients shown in Table 4 gives

$$T(K) = \frac{\left[\begin{array}{c} -3230 - 100P - 1402\mathrm{Mg}_{\#}^{ol} + 1933X_{CaO}^{melt} \\ +2612(X_{NaO_{0\cdot5}}^{melt} + X_{KO_{0\cdot5}}^{melt}) - 569X_{SiO_2}^{melt} \end{array}\right]}{\left(-1\cdot471 - \log_{10} KD_{Sc/V}^{ol/melt}\right)} \quad (3)$$

$$\log_{10} f_{O_2}(\Delta\mathrm{QFM}) = -7\cdot7 - \left(\frac{\log_{10} D_V^{ol/melt}}{0\cdot2639}\right) - \left\{\frac{\left[\begin{array}{c} 822 - 3328(1-\mathrm{Mg}_{\#}^{ol})^2 + 5326X_{KO_{0\cdot5}}^{melt} \\ +746(X_{CaO}^{melt} + X_{NaO_{0\cdot5}}^{melt}) - 3254(X_{SiO_2}^{melt} + X_{AlO_{1\cdot5}}^{melt}) \end{array}\right]}{0\cdot2639T}\right\} \quad (4)$$

$$\log_{10} f_{O_2}(\Delta\mathrm{NNO}) = -7\cdot0 - \left(\frac{\log_{10} D_V^{ol/melt}}{0\cdot2635}\right) - \left\{\frac{\left[\begin{array}{c} 1372 - 3389(1-\mathrm{Mg}_{\#}^{ol})^2 + 5318X_{KO_{0\cdot5}}^{melt} \\ +747(X_{CaO}^{melt} + X_{NaO_{0\cdot5}}^{melt}) - 3259(X_{SiO_2}^{melt} + X_{AlO_{1\cdot5}}^{melt}) \end{array}\right]}{0\cdot2635T}\right\} \quad (5)$$

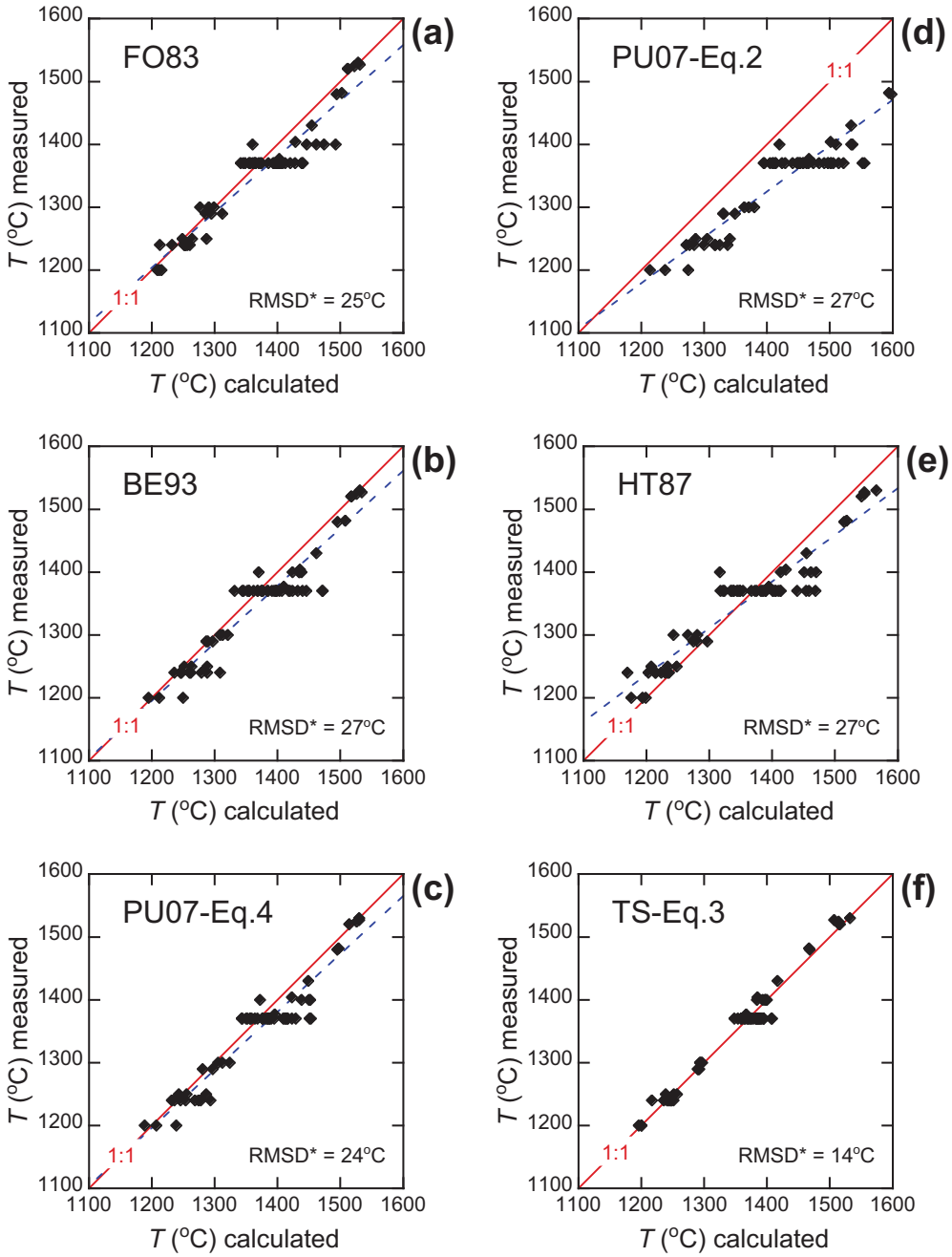

Fig. 6. Comparison between the temperatures measured in 66 experiments (selected out of the 189 reported in Fig. 5 to exclude those at high pressure, as well as compositions rich in alkalis and from Fe-free systems) with those calculated from various MgO-geothermometers and our new $KD^{ol/melt}_{Sc/V}$ calibration. Sources: FO83, Ford *et al.* (1983); BE93, Beattie (1993); PU07, Putirka *et al.* (2007); HT87, Helz & Thornber (1987); TS-Eq.3, this study, equation (3). RMSD* is the root mean square deviation calculated for the geothermometers after applying a correction for systematic error using a linear fit (shown by dashed line) through the data.

where temperature (T) is in Kelvin, pressure (P) is in GPa, $\log_{10} f_{O_2}$ is given relative to either QFM [equation (4)] or NNO [equation (5)] buffers, and mole fractions in the melt are calculated on a single-cation basis. We emphasize that the $D_V^{ol/melt}$ oxybarometer should be applied only within the calibrated range (i.e. QFM−4 to QFM+4) given that the partitioning relationship of this element with oxygen fugacity under more oxidized and reducing conditions must be different (i.e. $D_V^{ol/melt}$ gradually loses its sensitivity to oxygen fugacity).

Table 5: Example of temperature and oxygen fugacity calculation using the major and trace element (V, Sc and Y) composition of coexisting olivine and silicate melt

	Melt	Olivine	Melt mole fractions
SiO_2 (cg g^{-1})	49·94	38·73	$X(SiO_2)$ 0·4656
TiO_2	0·90	<0·01	$X(TiO_2)$ 0·0063
Al_2O_3	15·21	0·07	$X(AlO_{1·5})$ 0·1671
Cr_2O_3	0·05	0·06	$X(CrO_{1·5})$ 0·0004
FeO*	9·89	12·91	X(FeO) 0·0771
MnO	0·16	0·21	X(MnO) 0·0013
NiO	0·01	0·23	X(NiO) 0·0001
MgO	8·04	46·78	X(MgO) 0·1117
CaO	13·20	0·36	X(CaO) 0·1318
Na_2O	2·05	<0·01	$X(NaO_{0·5})$ 0·0371
K_2O	0·08	<0·01	$X(KO_{0·5})$ 0·0010
P_2O_5	0·08	<0·01	$X(PO_{2·5})$ 0·0006
Total	99·61	99·35	
Mg#	0·5917	0·8659	
V (μg g^{-1})	278·9 ± 2·8	9·58 ± 0·3	
Sc	37·5 ± 0·9	8·45 ± 0·24	
Y	18·0 ± 0·2	0·123 ± 0·007	
$KD_{Sc/Y}^{ol/melt}$	33·00 ± 2·28	(measured)	
$D_V^{ol/melt}$	0·0344 ± 0·0011	(measured)	
P (GPa)	0·10	(assumed)	
T (K) equation (3)	1460 ± 24	(calculated)	
ΔQFM equation (4)	0·87 ± 0·08	(calculated)	
ΔNNO equation (5)	0·17 ± 0·08	(calculated)	

Sample VG6820 (Pacific mid-ocean ridge basalt) from the Smithsonian Institute's collection.
*Total Fe given as FeO.

In Table 5 we present a practical example of the application of the $KD_{Sc/Y}^{ol/melt}$ geothermometer [equation (3)] and $D_V^{ol/melt}$ oxybarometer [equations (4) and (5)] to a mid-ocean ridge basaltic glass containing olivine microphenocrysts (Fig. 7). Major and trace element data for this sample (VG6820) were collected as described previously for the experiments. Assuming an olivine–melt equilibrium pressure of 0·1 GPa, we estimate a temperature of 1187°C, which is in agreement with the temperature of 1191°C calculated using the Ford *et al.* (1983) MgO-geothermometer, and a relative oxygen fugacity of QFM+0·87 (or NNO+0·17). Propagation of error on Sc, V and Y measurements gives a precision of 24°C and 0·08 $\log_{10} f_{O_2}$ units (one standard deviation).

Fe-XANES measurements on the silicate glass of sample VG6820 obtained at beamline I18, Diamond Light Source (unpublished data), indicate an $Fe^{3+}/\sum Fe$ content of ~0·13. This is considerably lower that the value of 0·20

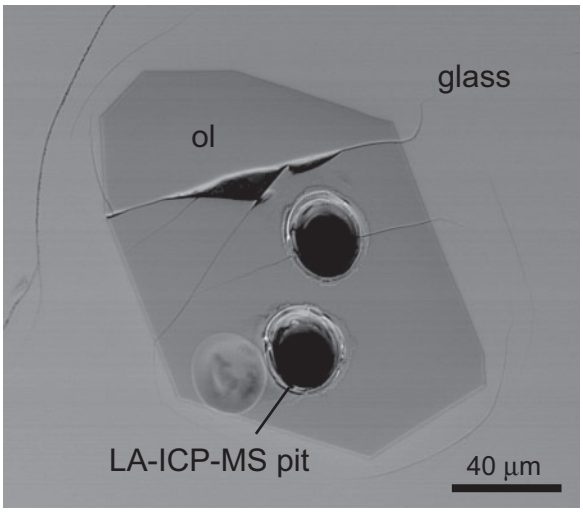

Fig. 7. Backscattered electron (BSE) image of a water-quenched mid-ocean ridge basalt (MORB) collected in the Pacific Ocean (from the Smithsonian Institute's collection) showing clear silicate glass surrounding an olivine phenocryst. Major and trace element compositions of the olivine and silicate glass are given in Table 5.

calculated by the algorithm of Kress & Carmichael (1991) assuming the relative oxygen fugacity of QFM+0·87 determined by our $D_V^{ol/melt}$ oxybarometer at 0·1 GPa and 1187°C. It should be noted that an error of ± 0·02 in the $Fe^{3+}/\sum Fe$ content determined by XANES on sample VG6820 translates to an uncertainty of ~0·4 $\log_{10} f_{O_2}$ units. Applying the calibration of Canil (2002), which does not account for the effect of temperature and composition on $D_V^{ol/melt}$ but was derived from experiments on near-natural basalts and komatiites, gives QFM + 0·41 and a calculated $Fe^{3+}/\sum Fe$ of 0·17, which is intermediate between the Fe-XANES measurement and our $D_V^{ol/melt}$ oxybarometer estimation. Similarly, $Fe^{3+}/\sum Fe$ calculated using our $D_V^{ol/melt}$ oxybarometer in combination with the model of Kress & Carmichael (1991) for olivine-hosted melt inclusion pairs from Agrigan (Marianas) and Jalopi Cone arc-related magmas reported by Kelley & Cottrell (2012) are on average 0·09 higher than the values measured for the silicate glasses by Fe-XANES. It is interesting to note, however, that the difference between the Fe^{2+}/Mg olivine/melt distribution coefficients determined for sample VG6820 ($KD_{Fe/Mg}^{ol/melt}$ = 0·224) and the canonical value of 0·30 (Roeder & Emslie, 1970) requires $Fe^{3+}/\sum Fe$ in the silicate melt of the order of 0·25, which is even higher than the value of 0·20 estimated by our $D_V^{ol/melt}$ oxybarometer calibration. Resolution of these discrepancies will require further work on many more samples.

ACKNOWLEDGMENTS

Constructive reviews by Cin-Ty Lee, Arno Rohrbach and Wim van Westrenen helped to improve this paper. Simon

Turner is gratefully acknowledged for handling the manuscript. We also thank Charlotte Allen and Robert Rapp for their assistance during LA-ICP-MS and electron microprobe analyses, respectively. The Department of Mineral Sciences of the Smithsonian Institution kindly provided the natural basalt sample used in this study.

FUNDING

This work was supported by the São Paulo Research Foundation—FAPESP (grant number 2010/05512-1 to G.M.) and by the Australian Research Council—ARC (grant number DP0771640 to H.O'N.).

SUPPLEMENTARY DATA

Supplementary data for this paper are available at *Journal of Petrology* online.

REFERENCES

Arndt, N. T. (1986). Differentiation of komatiite flows. *Journal of Petrology* **27**, 279–301.

Beattie, P. (1993). Olivine–melt and orthopyroxene–melt equilibria. *Contributions to Mineralogy and Petrology* **115**, 103–111.

Berry, A. J., Shelley, J. M. G., Foran, G. J., O'Neill, H. St.C. & Scott, D. R. (2003). A furnace design for XANES spectroscopy of silicate melts under controlled oxygen fugacities and temperatures to 1773 K. *Journal of Synchrotron Radiation* **10**, 332–336.

Bézos, A. & Humler, E. (2005). The $Fe^{3+}/\sum Fe$ ratios of MORB glasses and their implications for mantle melting. *Geochimica et Cosmochimica Acta* **69**, 711–725.

Blundy, J. & Wood, B. (1994). Prediction of crystal–melt partition coefficients from elastic moduli. *Nature* **372**, 452–454.

Burgisser, A. & Scaillet, B. (2007). Redox evolution of a degassing magma rising to the surface. *Nature* **445**, 194–197.

Canil, D. (1997). Vanadium partitioning and the oxidation state of Archaean komatiite magmas. *Nature* **389**, 842–845.

Canil, D. (2002). Vanadium in peridotites, mantle redox and tectonic environments: Archean to present. *Earth and Planetary Science Letters* **195**, 75–90.

Canil, D. & Fedortchouk, Y. (2001). Olivine–liquid partitioning of vanadium and other trace elements, with applications to modern and ancient picrites. *Canadian Mineralogist* **39**, 319–330.

Chase, M. W. (1998). *NIST-JANAF thermochemical tables*. Gaithersburg, MD: National Institute of Standards and Technology.

Christie, D. M., Carmichael, I. S. E. & Langmuir, C. H. (1986). Oxidation states of mid-ocean ridge basalt glasses. *Earth and Planetary Science Letters* **79**, 397–411.

Cottrell, E. & Kelley, K. A. (2011). The oxidation state of Fe in MORB glasses and the oxygen fugacity of the upper mantle. *Earth and Planetary Science Letters* **305**, 270–282.

Dauphas, N., Craddock, P. R., Asimow, P. D., Bennett, V. C., Nutman, A. P. & Ohnenstetter, D. (2009). Iron isotopes may reveal the redox conditions of mantle melting from Archean to Present. *Earth and Planetary Science Letters* **288**, 255–267.

De Hoog, J. C. M., Gall, L. & Cornell, D. H. (2010). Trace-element geochemistry of mantle olivine and application to mantle petrogenesis and geothermobarometry. *Chemical Geology* **270**, 196–215.

Eggins, S. M., Kinsley, L. P. J. & Shelley, J. M. G. (1998). Deposition and element fractionation processes during atmospheric pressure laser sampling for analysis by ICP-MS. *Applied Surface Science* **129**, 278–286.

Evans, K. A. (2012). The redox budget of subduction zones. *Earth-Science Reviews* **113**, 11–32.

Evans, T. M., O'Neill, H. St.C. & Tuff, J. (2008). The influence of melt composition on the partitioning of REEs, Y, Sc, Zr and Al between forsterite and melt in the system CMAS. *Geochimica et Cosmochimica Acta* **72**, 5708–5721.

Foley, S. F., Jacob, D. E. & O'Neill, H. St.C. (2011). Trace element variations in olivines from Ugandan potassic rocks as clues to the chemical characteristics of parental magmas. *Contributions to Mineralogy and Petrology* **162**, 1–20.

Ford, C. E., Russel, D. G., Craven, J. A. & Fisk, M. R. (1983). Olivine–liquid equilibria: Temperature, pressure and compositional dependence of the crystal/liquid cation partition coefficients for Mg, Fe^{2+}, Ca and Mn. *Journal of Petrology* **24**, 256–265.

Frost, D. J. (1998). Erratum to D. J. Frost and B. J. Wood (1997) 'Experimental measurements of the fugacity of CO_2 and graphite/diamond stability from 35 to 77 kbar at 925 to 1650°C' Geochimica et Cosmochimica Acta 61, 1565–1574. *Geochimica et Cosmochimica Acta* **62**, 725.

Frost, D. J. & Wood, B. J. (1997). Experimental measurements of the fugacity of CO_2 and graphite/diamond stability from 35 to 77 kbar at 925 to 1650°C. *Geochimica et Cosmochimica Acta* **61**, 1565–1574.

Helz, R. T. & Thornber, C. R. (1987). Geothermometry of Kilauea Iki lava lake, Hawaii. *Bulletin of Volcanology* **49**, 651–668.

Jarosewich, E., Nelen, J. A. & Norberg, J. A. (1980). Reference samples for electron microprobe analysis. *Geostandards and Geoanalytical Research* **4**, 43–47.

Jenner, F. E. & O'Neill, H. St.C. (2012). Major and trace analysis of basaltic glasses by laser-ablation ICP-MS. *Geochemistry, Geophysics, Geosystems* **13**, Q03003, doi:03010.01029/02011GC003890.

Kelley, K. A. & Cottrell, E. (2012). The influence of magmatic differentiation on the oxidation state of Fe in a basaltic arc magma. *Earth and Planetary Science Letters* **329–330**, 109–121.

Kress, V. C. & Carmichael, I. S. E. (1991). The compressibility of silicate liquids containing Fe_2O_3 and the effect of composition, temperature, oxygen fugacity and pressure on their redox states. *Contributions to Mineralogy and Petrology* **108**, 82–92.

Lee, C.-T. A., Leeman, W. P., Canil, D. & Li, Z. X. A. (2005). Similar V/Sc systematics in MORB and arc basalts: Implications for the oxygen fugacities of their mantle source regions. *Journal of Petrology* **46**, 2313–2336.

Lee, C.-T. A., Luffi, P., Le Roux, V., Dasgupta, R., Albarède, F. & Leeman, W. P. (2010). The redox state of arc mantle using Zn/Fe systematics. *Nature* **468**, 681–685.

Lee, C.-T. A., Luffi, P., Chin, E. J., Bouchet, R., Dasgupta, R., Morton, D. M., Le Roux, V., Yin, Q. & Jin, D. (2012). Copper systematics in arc magmas and implications for crust–mantle differentiation. *Science* **336**, 64–68.

Mallmann, G. & O'Neill, H. St.C. (2007). The effect of oxygen fugacity on the partitioning of Re between crystals and silicate melt during mantle melting. *Geochimica et Cosmochimica Acta* **71**, 2837–2857.

Mallmann, G. & O'Neill, H. St.C. (2009). The crystal/melt partitioning of V during mantle melting as a function of oxygen fugacity compared with some other elements (Al, P, Ca, Sc, Ti, Cr, Fe, Ga, Y, Zr and Nb). *Journal of Petrology* **50**, 1765–1794.

Métrich, N., Berry, A. J., O'Neill, H. St.C. & Susini, J. (2009). The oxidation state of sulfur in synthetic and natural glasses determined by X-ray absorption spectroscopy. *Geochimica et Cosmochimica Acta* **73**, 2382–2399.

O'Neill, H. St.C. (1987). Quartz–fayalite–iron and quartz–fayalite–magnetite equilibria and the free-energy of formation of

fayalite (Fe_2SiO_4) and magnetite (Fe_3O_4). *American Mineralogist* **72**, 67–75.

O'Neill, H. St.C. (2005). A method for controlling alkali–metal oxide activities in one-atmosphere experiments and its application to measuring the relative activity coefficients of $NaO_{0.5}$ in silicate melts. *American Mineralogist* **90**, 497–501.

O'Neill, H. St.C. & Eggins, S. M. (2002). The effect of melt composition on trace element partitioning: An experimental investigation of the activity coefficients of FeO, NiO, CoO, MoO_2 and MoO_3 in silicate melts. *Chemical Geology* **186**, 151–181.

O'Neill, H. St.C. & Pownceby, M. I. (1993). Thermodynamic data from redox reactions at high temperatures. I. An experimental and theoretical assessment of the electrochemical method using stabilized zirconia electrolytes, with revised values for the Fe–'FeO', Co–CoO, Ni–NiO and Cu–Cu_2O oxygen buffers, and new data for the W–WO_2 buffer. *Contributions to Mineralogy and Petrology* **114**, 296–314.

Putirka, K., Perfit, M., Ryerson, F. J. & Jackson, M. G. (2007). Ambient and excess mantle temperatures, olivine thermometry, and active vs. passive upwelling. *Chemical Geology* **241**, 177–206.

Roeder, P. L. & Emslie, R. F. (1970). Olivine–liquid equilibrium. *Contributions to Mineralogy and Petrology* **29**, 275–289.

Shannon, R. D. (1976). Revised effective ionic radii and systematic studies of interatomic distances in halides and chalcogenides. *Acta Crystallographica, Section A* **32**, 751–767.

Shearer, C. K., McKay, G., Papike, J. J. & Karner, J. M. (2006). Valence state partitioning of vanadium between olivine–liquid: Estimates of the oxygen fugacity of Y980459 and application to other olivine-phyric martian basalts. *American Mineralogist* **91**, 1657–1663.

Sossi, P. A. & O'Neill, H. St.C. (2011). Systematic underestimation of the oxidation state of MORB glasses. V. M. Goldschmidt Conference. *Mineralogical Magazine* **75**, 1915–1915.

Tuff, J. & O'Neill, H. St.C. (2010). The effect of sulfur on the partitioning of Ni and other first-row transition elements between olivine and silicate melt. *Geochimica et Cosmochimica Acta* **74**, 6180–6205.

Witt-Eickschen, G. & O'Neill, H. St.C. (2005). The effect of temperature on the equilibrium distribution of trace elements between clinopyroxene, orthopyroxene, olivine and spinel in upper mantle peridotite. *Chemical Geology* **221**, 65–101.